Impact of powder properties on deoxidation and densification of carbon steels during powder bed fusion – Laser beam

Citation for the original published paper (version of record):
Hearn, W., Cordova Gonzalez, L., Raza, A. et al (2024). Impact of powder properties on deoxidation and densification of carbon steels during powder bed fusion – Laser beam. Powder Technology, 431. http://dx.doi.org/10.1016/j.powtec.2023.119046

Powder Technology 431 (2024) 119046

Contents lists available at ScienceDirect

Powder Technology

journal homepage: www.journals.elsevier.com/powder-technology

Impact of powder properties on deoxidation and densification of carbon steels during powder bed fusion – Laser beam

William Hearn [a,*], Laura Cordova [a], Ahmad Raza [a], Anton Dahl-Jendelin [b], Eduard Hryha [a]

[a] Department of Industrial and Materials Science, Chalmers University of Technology, SE-41296 Gothenburg, Sweden
[b] RISE Research Institutes of Sweden, Argongatan 30, SE-53153 Mölndal, Sweden

HIGHLIGHTS

- Increased deoxidation at high energy input & carbon content.
- Deoxidation at high carbon content driven by C/O interaction at elevated temperature.
- High avalanche energy, break energy & D_{10} induce lack of fusion at low energy input.

GRAPHICAL ABSTRACT

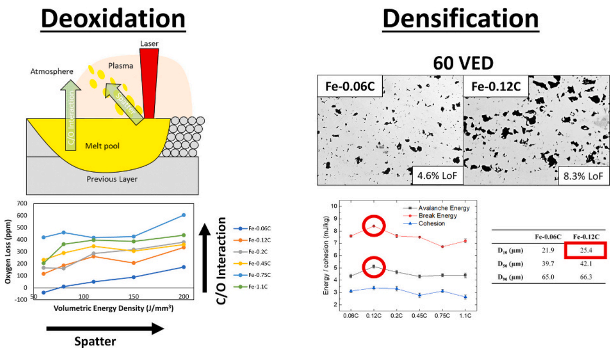

ARTICLE INFO

Keywords:
Additive manufacturing
Powder bed fusion
Carbon steel
Powder properties
Deoxidation
Densification

ABSTRACT

This work examined the influence of powder properties on deoxidation and densification of carbon steels during powder bed fusion-laser beam (PBF-LB) at compositions between 0.06 and 1.1 wt% C. Analysis revealed that deoxidation was greatest in alloys with high carbon content, reaching losses of up to 440–600 ppm at compositions of 0.75 and 1.1 wt% C. This behavior was not due to enhanced oxygen removal by spatter, as spatter in high carbon alloys had less oxygen pickup (~4% vs. ~27%) and formed smaller oxide layers (~42 nm vs. ~82 nm). Instead, it was due to the high oxygen affinity of carbon at elevated temperature, which resulted in formation of gaseous carbon oxides that were subsequently removed by the process atmosphere. Regarding densification, powders with high avalanche energy (>7.75 mJ/kg), break energy (>4.75 mJ/kg), and particle size distribution (D_{10} > 25 μm) were more likely to form lack of fusion porosity at low energy input.

1. Introduction

Powder bed fusion – laser beam (PBF-LB) is a novel additive manufacturing technique that uses thermal energy to selectively fuse regions of a powder bed. As PBF-LB develops, the introduction of new alloys is required to support its broader industrial implementation. Recently there has been push for the development of load-bearing materials like carbon steels, as they provide a combination of strength, toughness, and wear resistance that makes them suitable for structural applications [1]. This would help expand the materials portfolio of PBF-

---

* Corresponding author.
E-mail address: hearn@chlamers.se (W. Hearn).

https://doi.org/10.1016/j.powtec.2023.119046
Received 1 July 2023; Received in revised form 14 September 2023; Accepted 4 October 2023

LB in construction engineering, as materials in said industry remain limited [2].

Despite this interest, carbon steels are not readily available for PBF-LB as their high carbon content leads to a brittle martensitic microstructure that induces cracking defects. In order to make these alloys industrially viable, detailed process development is required to determine the conditions that produce high density and crack-free parts. As the presence of defects will deteriorate both final part quality, as well as mechanical properties [3–5].

Previous work by the authors [6] was able to define processing conditions (e.g., scan speed, laser power, hatch spacing) that produced crack-free carbon steels by PBF-LB. However, to continue the development of these alloys it is important to identify how other process inputs of PBF-LB affect final part quality.

While there are many inputs to consider for PBF-LB, one of the most prominent are the properties of the powder feedstock, which are known to affect process robustness [7–9]. Still, it is difficult to make clear correlations between the powder feedstock and part quality as there are many properties to consider. To date, most work has focused on the effect of the particle morphology and size distribution [10–13], with substantially less work focusing on the impact of other properties such as the bulk alloy chemistry or the rheological powder behavior.

Regarding the bulk alloy chemistry, past works have found that impurity elements like oxygen can have a deleterious effect on part quality, as more oxygen can increase part porosity [10,14] and decrease mechanical properties [14–17]. Typically, the oxygen content of parts produced by PBF-LB is high due to oxygen uptake during powder production, in addition to oxygen pick-up that occurs during powder re-use. The oxygen pick-up during re-use is primarily driven by the accumulation of spatter powder particles [18,19] which are typically oxidized [20] and agglomerated or spherical in shape [21–23]. Even though the amount of spatter can be controlled by adjusting the stability of the melt pool, they are still an unavoidable aspect of the process. Therefore, it is important to understand the mechanisms by which oxygen is reduced during PBF-LB to help mitigate this issue. Despite this, few studies have examined the various mechanisms of oxygen pick-up and removal during PBF-LB [24,25] and no such work has been conducted for carbon steels. This is important as carbon is a known reducing agent during sintering [26–28] and could enhance oxygen removal during PBF-LB.

As for the rheological powder behavior, past works have focused on its connection with powder flowability [29–31], as a high flowability can improve part density and mechanical properties [32]. One of the challenges with this approach is defining powder flowability in the first place, as it is not a specific property and is instead an umbrella term that describes the behavior of powder when subjected to stress or movement. This makes it a function of many different properties such as the particle size distribution, powder morphology, powder density, and surface chemistry [8,9,33,34].

Another difficulty is that the ability to estimate the powder flowability can be quite cumbersome, considering the required process set-up as new machine models and materials are developed. Solutions using a straight-forward rheological test like a Revolution Powder Analyzer (RPA) offer an interesting alternative to traditional powder flowability measurements, even though these RPA measurements might not represent the thin layer application in a powder bed fusion system [35]. Given the rotation of the drum when using a RPA, the analyzed powder is carried up the side causing it to collapse or avalanche by its own weight. This makes it possible to characterize the avalanche angle in a similar manner to the layer-based coating processes that were studied by Krantz et al. [36] that can subsequently be used to quantitatively distinguish between good and poor powder flow behavior [37]. Despite this promise, studies that have examined the relationship between rheological powder behavior and part quality remain limited, especially for carbon steels.

In the present study, the impact of bulk alloy chemistry and rheological powder behavior on the deoxidation and densification behavior of carbon steels during PBF-LB was studied at compositions between 0.06 and 1.1 wt% C. Analysis of the powders and produced parts involved a variety of characterization techniques including X-ray photoelectron spectroscopy (XPS), scanning electron microscopy (SEM), optical microscopy (OM), chemical analysis and a Revolution Powder Analyzer (RPA). The relationship between the bulk alloy chemistry and deoxidation behavior was determined using chemical analysis and correlated to results from XPS. While the relationship between powder properties and densification behavior was determined using part density measurements, in combination with rheological powder behavior measurements that were collected using a RPA.

2. Materials and methods

Six pre-alloyed, gas-atomized, carbon steel powders (supplied by Höganäs AB, Sweden) were examined during this study. The nominal composition of each powder is listed in Table 1. Measurement of the particle size distribution was conducted via laser diffraction using a Malvern Mastersizer 3000 (Malvern, UK). Prior to each measurement the powder was homogenized for 20 to 30 min, and each measurement was repeated five times.

The flow behavior of each powder grade was studied using a RPA (Mercury Scientific Inc., Newtown, CT). The test was carried out using a rotating and transparent drum filled with powder attached to an image acquisition system. The parameters were obtained from image analysis of the powder avalanches. A tapped powder sample of 29 cm^3 was used, where five measurements were made for each alloy composition and 150 avalanches were detected for each measurement. A drum insert with diameter of 50 mm was used at a rotation rate of 0.6 RPM, an image rate of 15 FPS and a preparation time of 30 s. As suggested by Spierings et al. [37], a fluidization treatment for conditioning of the powder was conducted prior to testing. The parameters obtained from this testing were the avalanche energy, break energy, cohesion, and avalanche angle. The avalanche energy is equivalent to the energy released during an avalanche, whereas the break energy gives an indication of the resistance of the powder to flow. This second parameter is closely related to the cohesion which is calculated from the shear stress created by the powder layer and provides an indication of whether the powder flows as individual particles or as agglomerates. The avalanche angle is measured from the powder free surface prior to the maximum potential energy with respect to the horizontal plane. In general, small avalanche energy, break energy, cohesion and avalanche angle are indications of good powder flow behavior [38,39]. The relative dynamic density was calculated by dividing the dynamic density by the theoretical density.

Using these powders, specimens with dimensions 5 × 5 × 5 mm^3 were produced using an EOS M100 machine (EOS GmbH, Germany). Said machine was equipped with Yb-fiber laser that had a maximum laser power of 200 W and a beam diameter of ~40 μm. During processing, an oxygen level of ~0.1% was maintained within the building chamber using Ar as the shielding gas. Additionally, no preheating of the building platform was applied. With regards to the scanning strategy, a stripe scan pattern was employed, along with a scan rotation angle of 67°. Specimens were produced at volumetric energy densities of 60, 80, 110, 150 and 200 J/mm^3 using a set hatch spacing (70 μm), layer thickness (20 μm) and laser power (110 W), see Table 2. These values were chosen based on a previous study by the authors on Fe-C steels

Table 1
Chemical composition of each carbon steel powder as provided by Höganäs AB.

	Fe-0.06C	Fe-0.12C	Fe-0.2C	Fe-0.45C	Fe-0.75C	Fe-1.1C
Fe (wt%)	Bal.	Bal.	Bal.	Bal.	Bal.	Bal.
C (wt%)	0.06	0.12	0.20	0.45	0.75	1.10
Si (wt%)	0.10	0.09	0.10	0.18	0.18	0.16
Mn (wt%)	0.06	0.09	0.09	0.15	0.08	0.08

Table 2
PBF-LB parameter sets used to produce the carbon steel specimens.

	Laser Power (W)	Layer Thickness (mm)	Hatch Spacing (mm)	Scan Speed (mm/s)	VED (J/mm^3)
1	110	0.02	0.07	1310	60
2				982	80
3				714	110
4				524	150
5				393	200

produced by PBF-LB [40].

Metallography of the produced specimens involved sectioning along the XZ direction, where the *Z*-direction related to the building direction while the X-direction related to the direction of gas flow. These specimens, along with powder particles, were further mounted and polished down to 1 μm using a Struers TegraPol machine (Struers, Denmark). After polishing, imaging of these specimens and powders was carried out using a Zeiss Axiovision 7 light optical microscope (Carl Zeiss AG, Germany), where images of the cross-sections were used to measure the density of the produced specimens with ImageJ software [41]. Analysis of the powders was also carried out using a Leo Gemini 1550 high-resolution scanning electron microscope (Carl Zeiss AG, Germany).

Further analysis of the powders was conducted via X-ray photoelectron spectroscopy (XPS) using an ULVAC-PHI 5500 machine (ULVAC-PHI Inc., Japan). For this study, a monochromatic Al Kα X-ray source was employed, where the analysis area was 300 × 300 m^2 and powder samples were mounted on an Indium plate template. The XPS data indicates a statistical average of 20 to 30 particles due to the vast measuring area. To determine the oxide layer thickness, Ar + ion etching was performed at a rate of around 5.2 nm/min. Ta_2O_5 foil was used to calibrate the etch rate. The pass energies used to collect the survey spectra and high-resolution narrow scans were 280 eV and 26 eV, respectively. Physical Electronics' MultiPak software was then used to conduct the spectrum analysis.

Lastly, the carbon content of the produced specimens and powders was measured via infrared absorption after combustion in an induction furnace using a LECO CS844 elemental analyzer (LECO Corporation, USA), in accordance with the EN ISO 15350 standard. While the oxygen content was measured by means of inert gas fusion using a LECO ON836 elemental analyzer (LECO Corporation, USA), in accordance with the EN 10276–2 standard. Due to the limited number of produced specimens, only a single measurement was conducted for the carbon and oxygen content respectively.

3. Results and discussion

3.1. Powder Properties & Bulk Alloy Chemistry

The particle morphology of the carbon steel powders was characterized using scanning electron microscopy (SEM). Said analysis revealed that each powder grade had a spherical morphology and contained limited satellite particles, see Fig. 1. Generally, this morphology is preferred for PBF-LB as it can improve powder flowability [12]. However, it is difficult to make general statements regarding the impact of powder morphology, as spherical powders can be beneficial for powder flow when dealing with coarse particles, while the opposite is true when dealing with finer particles [42]. Regardless, no noticeable difference in the morphology was observed when comparing the various carbon steel powders.

The particle size distribution (PSD), which can affect the bulk powder behavior [43,44], powder absorptivity [45], and properties of printed parts [13,46,47] revealed a somewhat similar size distribution for each carbon steel that ranged from ~20 to 65 μm, see Table 3. Some deviations in the PSD were observed at compositions of 0.12 wt% C and 1.1 wt% C, as these powders had an elevated D_{10} and D_{50}, see Table 3, and contained fewer fine particles. This ultimately led to a right shift of the PSD to coarser sizes, see Fig. 2.

Chemical analysis of the powders was carried out to measure the carbon and oxygen content in the virgin state. Generally, these

Table 3
Particle size distribution for the examined carbon steel powders.

	Fe-0.06C	Fe-0.12C	Fe-0.2C	Fe-0.45C	Fe-0.75C	Fe-1.1C
D_{10} (μm)	21.9	25.4	21.9	23.1	21.7	25.8
D_{50} (μm)	39.7	42.1	40.5	40.2	40.0	41.6
D_{90} (μm)	65.0	66.3	66.3	65.0	65.4	64.8

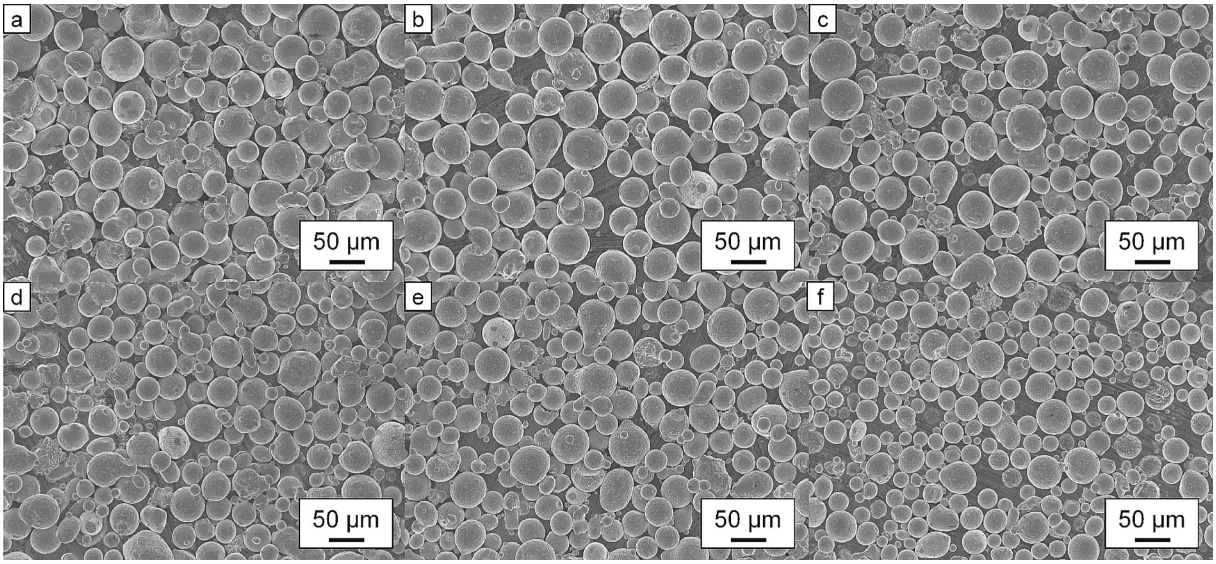

Fig. 1. SE SEM images of: a) Fe-0.06C powders, b) Fe-0.12C powders, c) Fe-0.2C powders, d) Fe-0.45C powders, e) Fe-0.75C powders and f) Fe-1.1C powders.

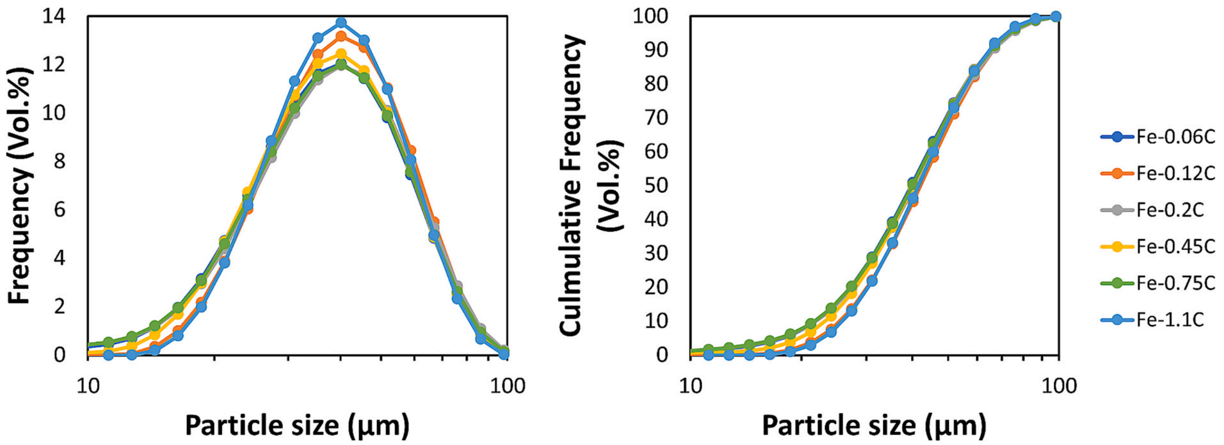

Fig. 2. Frequency and cumulative frequency of the particle size for the examined carbon steel powders.

Table 4
Carbon and oxygen content for each carbon steel powder as measured by combustion and inert gas fusion analysis.

	Fe-0.06C	Fe-0.12C	Fe-0.2C	Fe-0.45C	Fe-0.75C	Fe-1.1C
C in Powder (ppm)	650	1310	2090	4640	7660	11,700
O in Powder (ppm)	880	590	570	480	700	480

measurements found that powders with higher carbon content had lower oxygen content, see Table 4. However, the 0.75 wt% C powder had an elevated oxygen content that exceeded most of the other alloys.

Overall, the presented results show that changes in the bulk alloy chemistry did not noticeably alter the morphology of the produced powders. However, the carbon content does influence the oxygen level of the powder, as generally more carbon leads to less oxygen.

3.2. Rheological powder behavior

Fig. 3 shows the values obtained from testing of the carbon steel powders using a RPA. The avalanche energy, break energy and cohesion are represented in Fig. 3a. In general, all powders exhibited similar values for these parameters indicating the limited impact of alloy composition. At a composition of 0.12 wt% C a relatively high avalanche and break energy was measured, indicating that this powder grade had a worse powder flow behavior and required more energy to break the avalanche. In terms of the avalanche angle, see Fig. 3b, some differences were observed as there was a tendency for the avalanche angle to reduce by up to 2.75° as the carbon content increased, indicating an improvement in powder flow behavior [30]. Additionally, it was found that powders with finer particle size distributions (e.g. Fe-0.06 wt% C, Fe-0.2 wt% C and Fe-0.75 wt% C) had slightly larger avalanche angles than the alloys with similar carbon content. The largest values for the relative dynamic energy were observed for powders with 0.12 wt% C and 0.45C wt% C, see Fig. 3c, which is positive for a homogenous powder bed. However, the ability of the powder to spread as a thin layer will determine the packing density on the building platform. In addition, the difference in the relative dynamic energy was limited when comparing

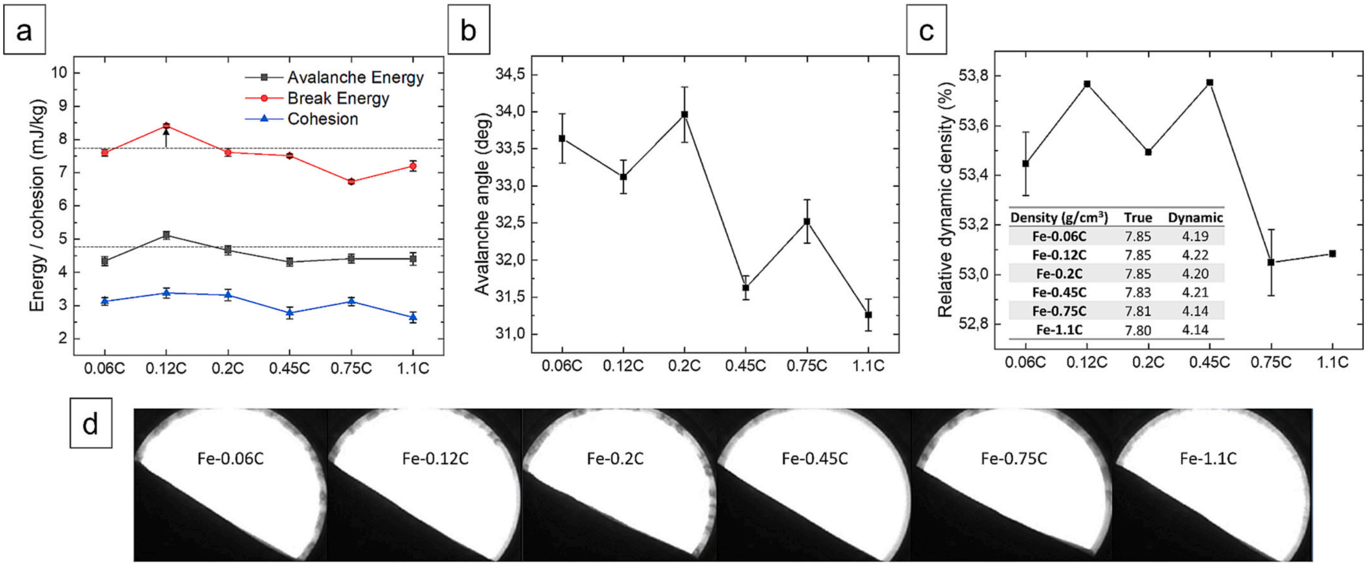

Density (g/cm^3)	True	Dynamic
Fe-0.06C	7.85	4.19
Fe-0.12C	7.85	4.22
Fe-0.2C	7.85	4.20
Fe-0.45C	7.83	4.21
Fe-0.75C	7.81	4.14
Fe-1.1C	7.80	4.14

Fig. 3. Rheological properties of the studied carbon steel powders: (a) avalanche energy, break energy and cohesion, (b) avalanche angle, (c) relative dynamic density, (d) morphology of the powder avalanche slope. In figure (d) the powder avalanche is the black region, while the area inside the of drum without powder is the white region.

the different carbon steel alloys. Lastly, Fig. 3d shows a snapshot of the powder layer prior to an avalanche. These pictures reveal low cohesiveness attributed to the particle morphology and size distribution as was discussed by Chavez Montes et al. [48]. Overall, despite a slight reduction in the avalanche angle with increasing carbon content and a slightly larger avalanche angle at finer PSD, the rheological behavior of the powders was not noticably different when comparing the various alloy compositions.

3.3. Deoxidation during PBF-LB

Although PBF-LB is considered an inert process due to the constant flow of shielding gas, there is still a residual oxygen level of ~0.1% within the building chamber, in addition to oxygen that can originate from the powder feedstock. These factors combined with the high temperatures of PBF-LB can lead to alloying elements with high oxygen affinity reacting to form oxides during the process [24,25,42].

To examine this potential formation of oxides, as well as the change in bulk alloy chemistry, the difference in carbon and oxygen from powder to part was measured for each carbon steel, see Fig. 4. For all alloys, decarburization from powder to part was observed regardless of the initial carbon content or the applied VED, with the relative carbon loss ranging from ~1 to 50%. The total carbon loss generally increased as the VED increased and exceeded the total oxygen loss at compositions ≤0.2 wt% C but was than the total oxygen loss at compositions ≥0.45 wt% C, see Table 5. Despite this, it was difficult to make clear correlations between the carbon loss and the initial carbon content, as the greatest loss of 300 to 440 ppm occurred at a composition of 0.75 wt% C, while the lowest loss of 100 to 200 ppm occurred at a composition of 1.1 wt% C.

There was also oxygen loss in all specimens from powder to part except for the 0.06 wt% C alloy produced at 60 J/mm^3, see Fig. 4. Just as with carbon, the degree of oxygen loss generally increased as the VED increased. However, unlike carbon, the oxygen loss was also influenced by the carbon content, as alloys with more carbon typically experienced greater oxygen loss, regardless of the applied VED. Additionally, the final oxygen content of the produced parts would decrease with increasing carbon content, even if the initial oxygen content of the powder was higher, see Table 6. Work by Haines et al. [24] hypothesized that the dominant mechanism of oxygen removal during PBF-LB was the formation of spatter particles. This can partially explain the enhanced loss of oxygen with increasing VED, as larger energy inputs typically induce the formation of more spatter [49]. However, it is unclear if this can describe the increased loss of oxygen as the carbon content increased.

To see if this tendency was due to greater oxygen removal by individual spatter particles, additional analysis was carried out on virgin and spatter particles from the 0.06 wt% C and 0.75 wt% C alloys. The variation between the spatter and virgin powders is illustrated in Fig. 5. Fig. 5a shows the morphology of virgin 0.06 wt% C powder. In comparison, the spatter particles from the 0.06 wt% C and 0.75 wt% C alloys indicate the presence of many bright particles. Higher magnification images of this spatter, see Fig. 5d, indicate the formation of fine oxide particulates that cover the particle surface. The number of highly oxidized particles from the sampled spatter was greater at a composition of 0.06 wt% C than at a composition of 0.75 wt% C, see Fig. 5b and Fig. 5c. This provides an indication that spatter within the higher carbon alloy was less likely to oxidize.

Table 5
Carbon content in ppm for the powder feedstock and specimens produced at VEDs of 60, 80, 110, 150 and 200 J/mm^3.

	Fe-0.06C	Fe-0.12C	Fe-0.2C	Fe-0.45C	Fe-0.75C	Fe-1.1C
Powder	650	1310	2090	4640	7660	11,700
60 J/mm^3	540	1140	1910	4490	7360	11,600
80 J/mm^3	470	1060	1810	4360	7320	11,600
110 J/mm^3	450	1040	1720	4350	7280	11,600
150 J/mm^3	400	970	1690	4330	7230	11,500
200 J/mm^3	310	890	1660	4380	7220	11,500

Table 6
Oxygen content in ppm for the powder feedstock and specimens produced at VEDs of 60, 80, 110, 150 and 200 J/mm^3.

	Fe-0.06C	Fe-0.12C	Fe-0.2C	Fe-0.45C	Fe-0.75C	Fe-1.1C
Powder	880	590	570	480	700	480
60 J/mm^3	920	470	400	250	290	280
80 J/mm^3	870	400	410	190	250	120
110 J/mm^3	830	330	280	130	290	90
150 J/mm^3	790	380	250	170	280	100
200 J/mm^3	710	250	190	120	100	50

XPS survey spectra can provide information regarding the surface chemistry of the powder samples and was measured for selected virgin and spatter particles from the 0.06 wt% C and 0.75 wt% C alloys, see Fig. 6. Here, iron peaks from Fe2p and Fe3p, along with carbon (C1s) and oxygen (O1s) peaks are observed. All samples apparently show a similar spectra without any sign of contamination.

Next, a thorough depth profile analysis was carried out on relevant narrow spectra to reveal the nature and thickness of oxides within the powders. Depth profile analysis from the Fe2p narrow spectra is presented in Fig. 7. The virgin 0.06 wt% C powder shows no metal peak at ~707 eV on the as-received surface, with it starting to appear after 15 nm of etching, see Fig. 7a. At an etched depth of 30 nm the Fe2p$_{3/2}$(0)

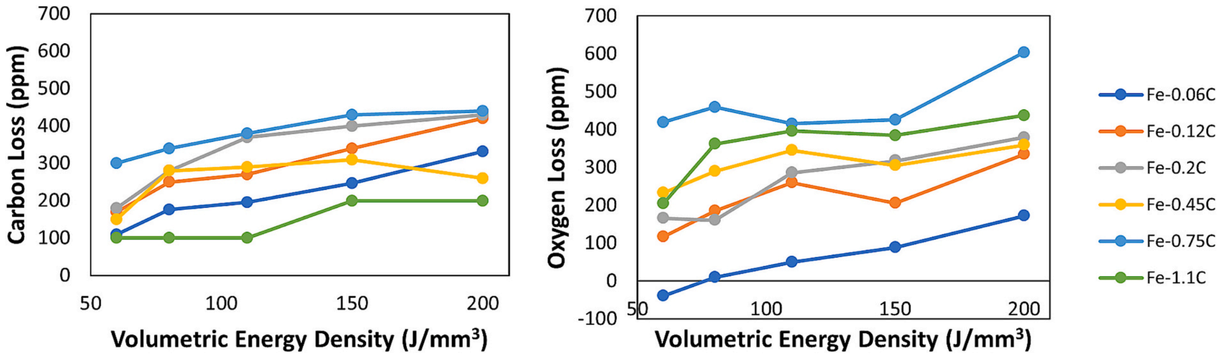

Fig. 4. Carbon loss (left) and oxygen loss (right) from the powder to part for the examined carbon steels.

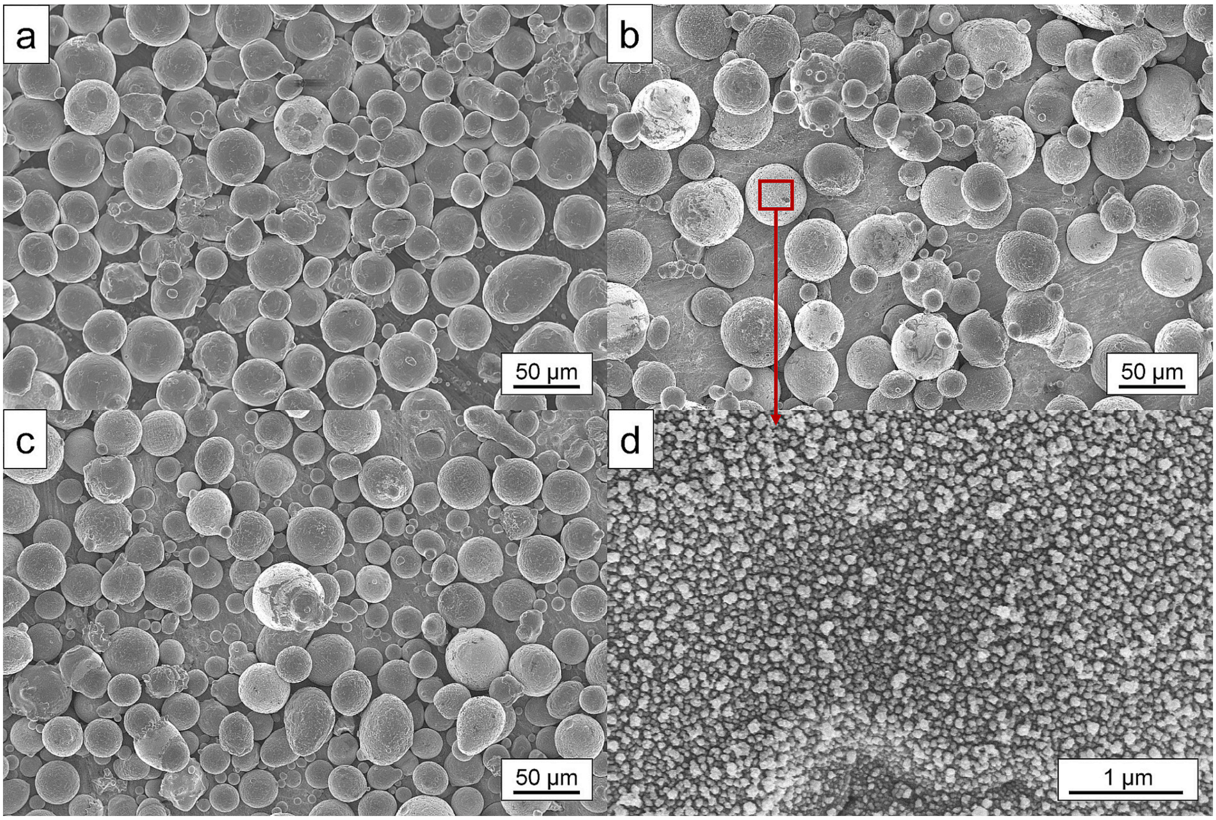

Fig. 5. SE SEM images comparing of the morphology of virgin Fe-0.06C sample (a) with the spatter samples from Fe-0.06C (b) and Fe-0.75C (c). Image (d) is a high magnification image of a spatter particle shown in (b) from the Fe-0.06C spatter sample.

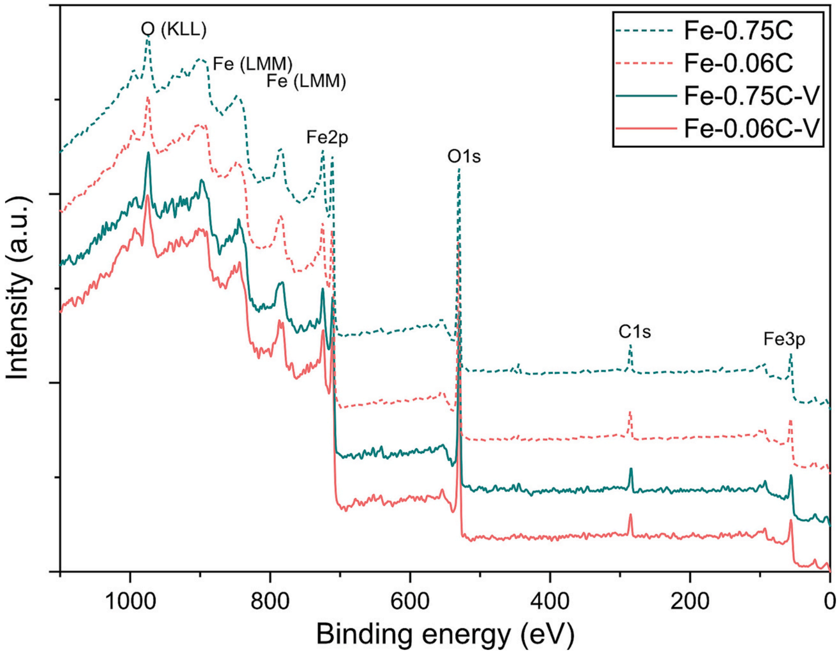

Fig. 6. Survey scan of the as-received surface from virgin (Fe-0.06-V & Fe-0.75C-V) and spatter powders (Fe-0.06C & Fe-0.75C) from the Fe-0.06C and Fe-0.75C alloys.

peak, corresponding to metal state, dominated the oxide peak that was composed by Fe2p$_{3/2}$(II) at ~710 eV and Fe2p$_{3/2}$(III) at ~711.1 eV. In comparison, the narrow spectra from the 0.06 wt% C spatter found that the Fe2p$_{3/2}$(0) peak appeared after an etched depth of 50 nm and dominated the oxide peak after an etched depth of 85 nm, see Fig. 7b. This highlights the high surface oxidation of spatter when compared to virgin powder.

Comparing the two virgin powders also showed an interesting contrast, as the Fe2p$_{3/2}$(0) peak appeared at smaller etched depths for the 0.75 wt% C alloy, see Fig. 7c, indicating a smaller oxide layer.

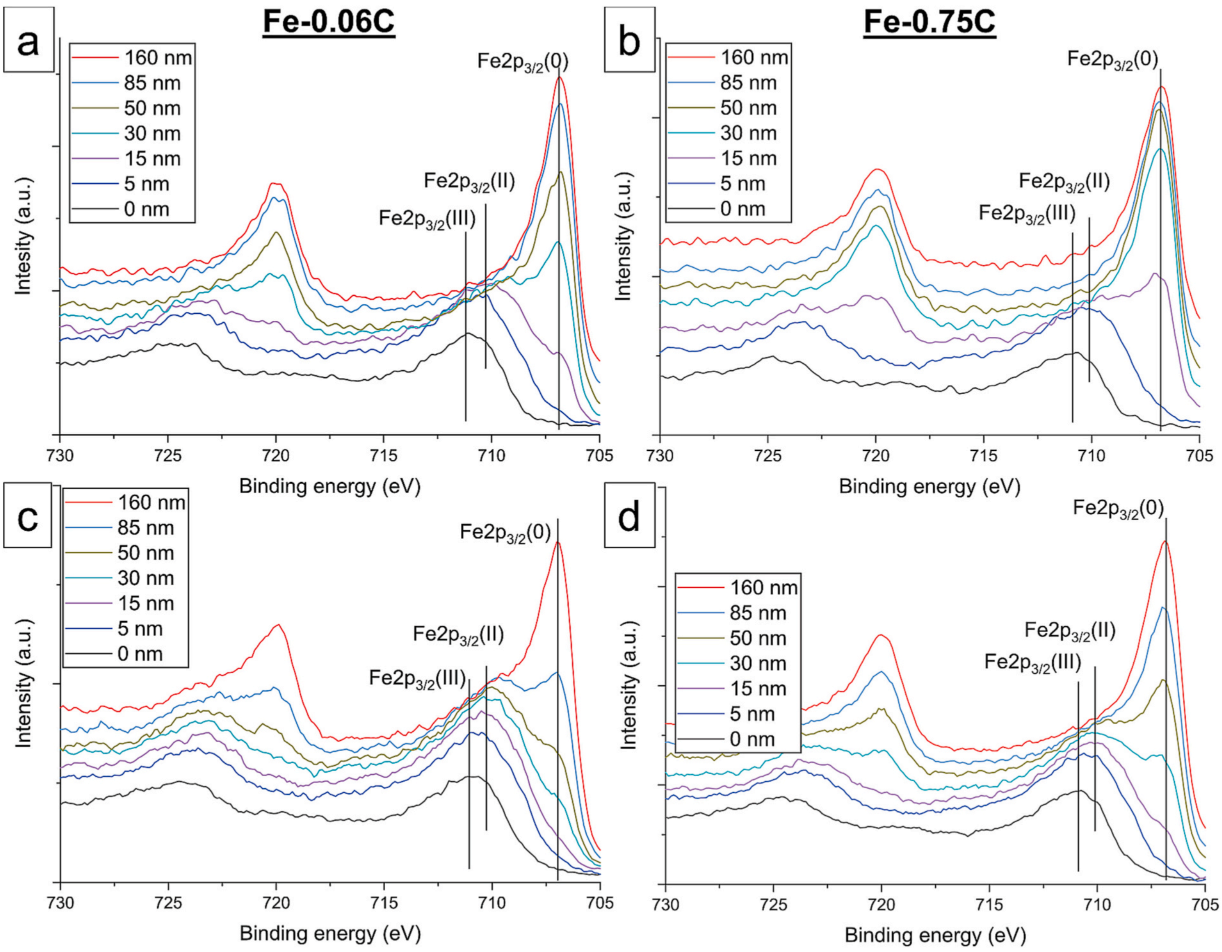

Fig. 7. A comparison of XPS narrow spectra of Fe2p3/2 of virgin a) Fe-0.06C and b) Fe-0.75C with spatter samples of c) Fe-0.06C and d) Fe-0.75C.

Moreover, evaluation of the 0.75 wt% C spatter revealed an increase in the oxide layer thickness when compared to the virgin powder, see Fig. 7d, as the Fe2p$_{3/2}$(0) peak appeared at larger etched depths. However, a comparison of spatters from the 0.06 wt% C and 0.75 wt% C alloys showed that the Fe2p$_{3/2}$(0) peak appeared again at smaller etch depths for the 0.75 wt% C alloy, indicating a smaller oxide layer. This reaffirms the observations from SEM where a great number of oxidized particles were found from the collected spatter of the 0.06 wt% C alloy.

The effect of spatter formation on carbon loss, oxygen pick up and increase in oxide layer thickness is presented in Fig. 8. Fig. 8a, shows a comparison of the carbon content for virgin and spatter particles. Results found that the carbon content is similar for the virgin and spatter particles from the 0.06 wt% C alloy, which indicates that carbon couldn't play a role in reducing the extent of oxidation due to its minute concentration. In contrast, a ~ 4% drop was observed in the carbon content of the 0.75 wt% C spatter, which presumably occurred due to the carbon loss assisted by the oxidation of the spatter particles.

The effect of carbon loss on oxygen pick-up of the spatters is shown in Fig. 8b. Spatter from the 0.06 wt% C alloy, which showed no carbon loss, displayed a ~ 27% increase in oxygen. While the spatter from the 0.75 wt% C alloy displayed a mere ~4% increase in oxygen. This verifies that carbon within the 0.75 wt% C alloy reacted with oxygen during spatter oxidation, resulting in formation of gaseous carbon oxides (CO and CO_2) that were subsequently removed by the process gas. This allows for a decrease in surface oxidation of the spatter particles, as was observed during PBF-LB of more sensitive carbon-free alloys [18,23].

Lastly, the oxide layer thickness was measured using the intensity of Fe2p$_{3/2}$(0) peak, as was reported by Raza et al. [18] and Gruber et al. [50]. The oxide layer thickness of virgin powder from the 0.06 wt% C alloy was substantially larger (~25 nm) than the 0.75 wt% C alloy (~15 nm). Spatters from both alloys showed a similar trend, as the oxide layer thickness was again larger for the 0.06 wt% C alloy (~82 nm) than the 0.75 wt% C alloy (~42 nm). These results also indicated that there was an approximate 3-fold increase in the oxide layer thickness from virgin to spatter particles, which is not as significant in the oxygen pickup measurement as not all the powders from the sampled spatter were heavily oxidized.

These results from XPS indicate that the increased loss of oxygen with increasing carbon content was not due to improved oxygen removal by individual spatter particles. In fact, the results showed the opposite as increasing the carbon content not only decreased the amount of oxygen within the spatter particles but also made them less oxidized. This means that a different mechanism is inducing this change during the process.

An important oxygen removal mechanism during PBF-LB is the reduction of oxygen at the surface of the melt pool. Here, oxygen can react with other elements at high temperatures to form constituents that will be removed by the flow of the shielding gas. In the examined carbon steels, the major alloying elements were carbon, manganese, and silicon. Out of these elements, carbon has the highest activity to react with oxygen at high temperature, where the driving force for the reaction of carbon and oxygen will become progressively more favoured as the temperature increases [51]. Above the Boudouard equilibrium (~720 °C) the expected product of this reaction will be carbon monoxide (CO) as it has a larger thermodynamic driving force to from when compared to carbon dioxide (CO_2) due to its more negative free energy change [26]. This preferential formation of CO during PBF-LB of carbon steel was observed by Hilzenthaler et al. [52] as the CO content within

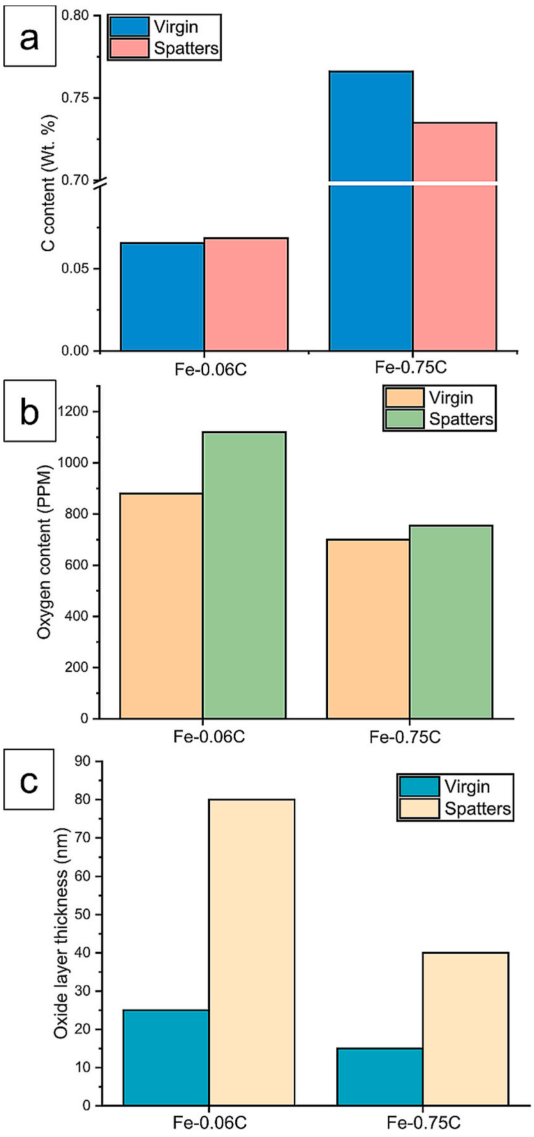

Fig. 8. Comparisons between bulk chemistry of virgin and spatter powders showing a) carbon content, b) oxygen content and c) oxide layer thickness determined by XPS.

the build chamber experienced a step-like growth during the process, while the CO_2 content remained unchanged.

The reduction of oxygen by carbon remains relatively unexplored for PBF-LB. However, its effect is more thoroughly understood from classical powder metallurgy where carbon is known to act as a strong reducing agent during sintering. During sintering under inert atmospheres, the reduction of oxygen by carbon takes place in two stages. First, the reduction of powder surface oxides occurs, leading to the pronounced formation of CO at temperatures between 640 and 730 °C [53]. This is then followed by the reduction of internal oxides at higher temperatures, as these oxides must first diffuse to the surface prior to reacting with carbon [54]. Despite the substantially faster kinetics and higher peak temperatures of PBF-LB, this deoxidation is still likely to occur and become more prominent as the carbon content increases.

The enhanced reduction of oxygen by carbon is a positive finding, as it removes a harmful impurity element and can be used to mitigate relatively high oxygen content within the powder. Additionally, it seems that increasing the carbon content can reduce the oxidation of spatter particles which can alleviate oxygen pick-up during powder re-use, a known issue for the recycling of low-alloy steels during PBF-LB [19]. At the same time, the noticeable loss of carbon during PBF-LB must be accounted for to ensure that the produced part has the desired composition after processing.

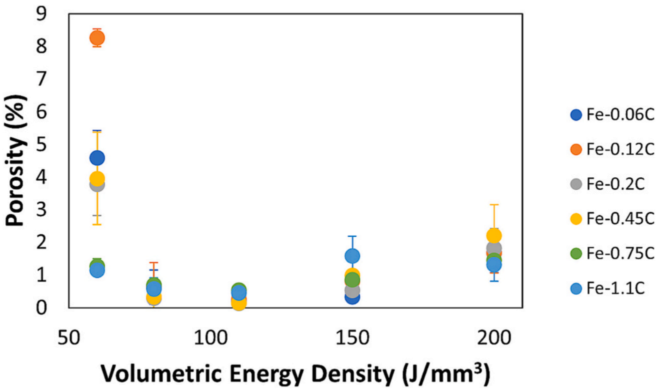

Fig. 9. Change in part porosity with VED for the examined carbon steels.

3.4. Densification

The percentage of porosity was measured and plotted for each of the produced specimens, see Fig. 9. At the lowest VED of 60 J/mm^3 the specimens had the highest percentage of porosity (up to ~8%) that related to large and irregular lack of fusion pores, see Fig. 10. Generally, the amount of lack of fusion decreased as the carbon content increased, as previous work by the authors [6] found that this would reduce the liquid viscosity and surface tension, enhancing the melt pool wettability and flow. Similar improvements in melt pool wettability were reported by Nakamoto et al. [55]. An additional benefit with increasing carbon content was the enhanced reduction of oxygen, see Table 6, as this indicates a reduced presence of oxides within the melt pool improving its wettability, as a liquid will not wet surface oxide films [56].

Despite this, the presence of lack of fusion porosity was most prevalent at a composition of 0.12 wt% C, even when compared to the 0.06 wt% C composition that had a lower carbon content and a higher oxygen content, see Table 4. Looking at the bulk behavior of the 0.12 wt% C alloy, it had an elevated avalanche and break energy when compared to the other carbon steels, see Fig. 3a, indicating a reduced powder flow behavior. Additionally, the 0.12 wt% C alloy had a coarser PSD especially when examining the D_{10}, see Fig. 2 and Table 3. It is likely that these factors enhanced the formation of lack of fusion porosity during PBF-LB, as the reduced powder flow behavior limited its ability to form a cohesive layer. While the coarser PSD meant that there were fewer fine particles to fill in the voids between coarser particles. Similar findings were reported by Simchi [10,11] and Haferkamp et al. [12] where coarser PSDs led to an increase in part porosity at high scan speeds. It should be noted that a similarly coarse PSD was observed at a composition of 1.1 wt% C. However, the lower avalanche energy, break energy and enhanced melt pool wettability helped mitigate this issue, allowing this alloy to avoid the widespread formation of lack of fusion porosity.

The porosity found in specimens produced at 80 and 110 J/mm^3 was limited (< 1%) and primarily related to small circular pores, see Fig. 10. These porosities are considered to originate from metallurgical pores or from entrapped gas porosity that is transferred from the powder feedstock [57]. Analysis of powder cross-sections revealed limited internal porosity for each of the powder grades, see Fig. 11. In addition, noticeable differences in the number of these small pores could not be distinguished when comparing the carbon steels, see Fig. 9. These results indicate that the alloy composition had a negligible effect on the formation of these small porosities during PBF-LB.

At compositions of 0.06 wt% C and 0.12 wt% C, some larger pores related to lack of fusion porosity were still observed in specimens produced at 80 J/mm^3, see Fig. 10. However, no noticeable difference in the

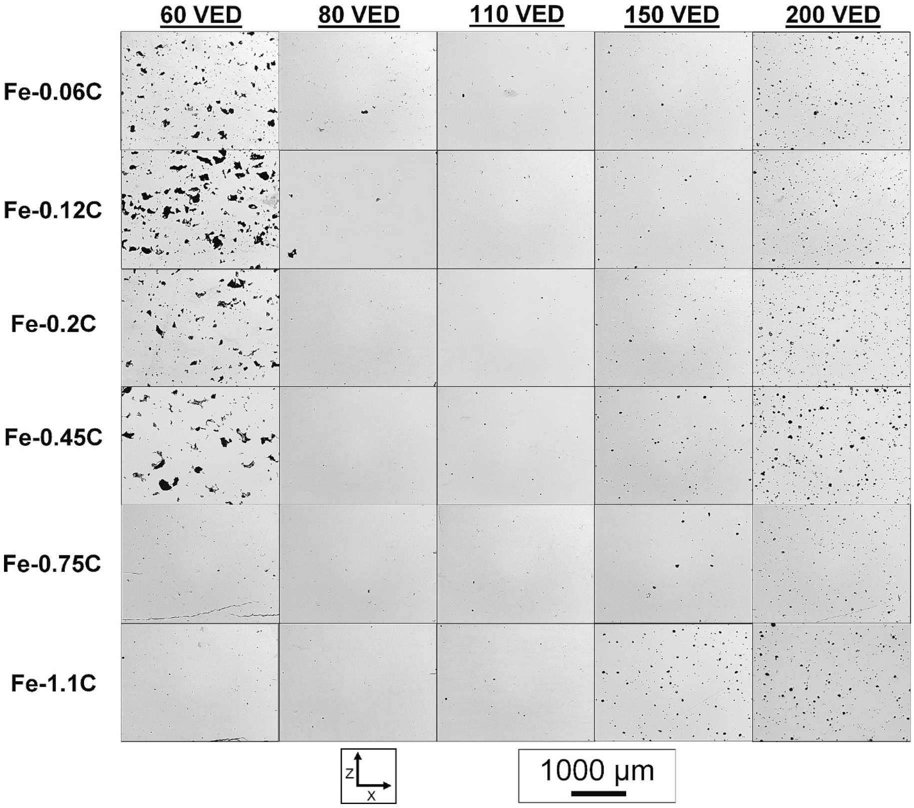

Fig. 10. Characteristics specimen cross-sections outlining the observed porosity for the carbon steels produced at VEDs of 60, 80, 110, 150 and 200 J/mm^3.

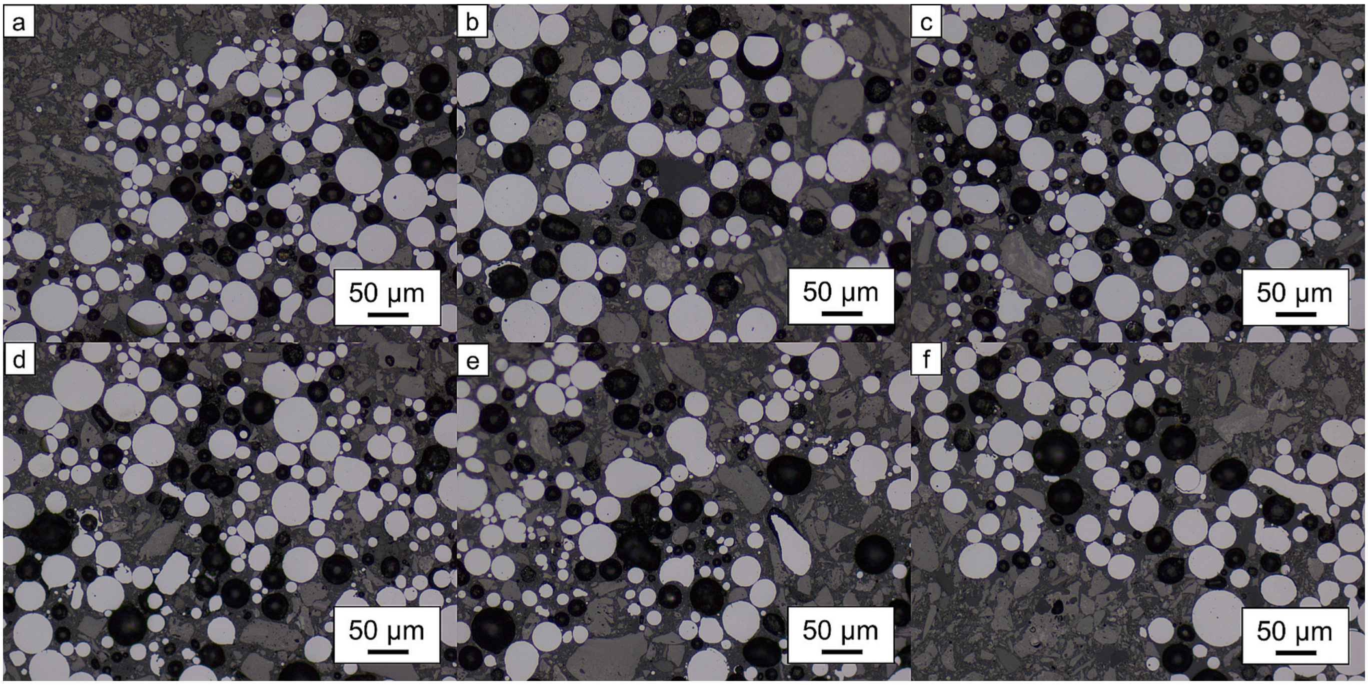

Fig. 11. Polished powder cross-sections for: a) Fe-0.06C powders, b) Fe-0.12C powders, c) Fe-0.2C powders, d) Fe-0.45C powders, e) Fe-0.75C powders, and f) Fe-1.1C powders.

amount of said porosity was observed when comparing the two alloys, see Fig. 9, which is in contrast to the trend observed at 60 J/mm^3. This indicates that once sufficiently large VEDs are applied, issues related to reduced powder flow behavior and fewer fine particles do not seem to drastically effect the formation of lack of fusion porosity.

4. Conclusions

The present study examined the impact of various powder properties on the deoxidation and densification behavior of carbon steels during PBF-LB at compositions between 0.06 and 1.1 wt% C and at VEDs between 60 and 200 J/mm^3. The main findings can be summarized as follows:

- The composition of the carbon steels did not noticeably influence either the morphology or the PSD of the powder feedstock. However, it did affect the initial oxygen content, as increasing the carbon content would decrease the oxygen content by up to 400 ppm.
- The rheological powder behavior was relatively unaffected by changes in alloy composition or PSD. Except for the avalanche angle, which decreased by up to 2.75° as the carbon content increased and was generally larger for powders with finer PSD at similar carbon content. This indicates a slight improvement in powder flow behavior as the carbon content increases or when using coarser PSD.
- In terms of part processing, the loss of carbon and oxygen was observed during PBF-LB for most specimens. Typically, the loss of both elements increased as the VED increased, with the carbon loss reaching up to 200 to 440 ppm and the oxygen loss reaching up to 170 to 600 ppm at the highest VED of 200 J/mm^3.
- The oxygen loss during PBF-LB also increased as the carbon content increased, reaching losses of up to 440 to 600 ppm at compositions of 0.75 and 1.1 wt% C. This increased deoxidation was not due to enhanced oxygen removal by individual spatter particles, as spatter from higher carbon alloys had less oxygen pick-up, formed smaller oxide layers ($\sim$42 nm vs. $\sim$82 nm) and was less likely to oxidize. Instead, it was connected to the reaction between oxygen and carbon at elevated temperature, which resulted in the formation of gaseous carbon oxides that were subsequently removed by the process atmosphere.
- In terms of densification, the properties and rheological behavior of the powder feedstock were found to influence the formation of lack of fusion porosity. As powders with high avalanche energy ($>$ 7.75 mJ/kg), break energy ($>$ 4.75 mJ/kg) and PSD ($D_{10} > 25$ μm), were more likely to form said defects at low VED. It was possible to mitigate these issues related to poor powder flow behavior and coarse PSD but only after VEDs $\geq$80 J/mm^3 were applied.

Funding

The work was preformed within the framework of the Centre for Additive Manufacturing – Metal (CAM^2), hosted by Chalmers University of Technology and supported by the Swedish Governmental Agency of Innovation Systems (Vinnova).

CRediT authorship contribution statement

William Hearn: Conceptualization, Methodology, Investigation, Writing – original draft, Writing – review & editing. **Laura Cordova:** Conceptualization, Investigation, Writing – original draft, Writing – review & editing. **Ahmad Raza:** Investigation, Writing – original draft. **Anton Dahl-Jendelin:** Investigation. **Eduard Hryha:** Conceptualization, Funding acquisition, Writing – review & editing, Supervision.

Declaration of Competing Interest

The authors declare that they have no known competing financial interests or personal relationships that could have appeared to influence the work reported in this paper.

Data availability

Data will be made available on request.

Acknowledgements

This study was conducted in the frame of the Centre for Additive Manufacturing – Metal (CAM^2), supported by the Swedish Governmental Agency of Innovation Systems (Vinnova). The authors would also like to thank and acknowledge Höganäs AB for providing the carbon steel powders that were examined during this work.

References

[1] A.I.H. Committee, ASM Handbook, Volume 01 - Properties and Selection: Irons, Steels, and High-Performance Alloys, ASM International, 1990.
[2] A.M.G. Issayev, E. Shehad, S. Sarfraz, A critical review of 3D printing and digital manufacturing in construction engineering, Rapid Prototyp. J. 28 (7) (2022) 1312–1324.
[3] P. Åkerfeldt, Additive Manufacturing of Ti-6Al-4V: Relationship between Microstructure, Defects and Mechanical Properties, Luleå University of Technology, Luleå, 2016.
[4] N. Larrosa, W. Wang, N. Read, M. Loretto, C. Evans, J. Carr, U. Tradowsky, M. Attallah, P. Withers, Linking microstructure and processing defects to mechanical properties of selectively laser melted AlSi10Mg alloy, Theor. Appl. Fract. Mech. 98 (2018) 123–133.
[5] Y. Zhou, E. Abbara, D. Jiang, A. Azizi, M. Poliks, F. Ning, High-cycle fatigue properties of curved-surface AlSi10Mg parts fabricated by powder bed fusion additive manufacturing, Rapid Prototyp. J. 28 (7) (2022) 1129–1143.
[6] W. Hearn, E. Hryha, Effect of carbon content on the processability of Fe-C alloys produced by laser based powder bed fusion, Front. Mater. 8 (2022).
[7] T. DebRoy, H. Wei, J. Zuback, T. Mukherjee, J. Elmer, J. Milewski, A. Beese, A. Wilson-Heid, A. De, W. Zhang, Additive manufacturing of metallic components – process, structure and properties, Prog. Mater. Sci. 92 (2018) 112–224.
[8] S. Vock, B. Klöden, A. Kirchner, T. Weissgärber, B. Kieback, Powders for powder bed fusion: a review, Progr. Add. Manufact. 4 (4) (2019) 383–397.
[9] A. Sutton, C. Kriewall, M. Leu, J. Newkirk, Powder characterisation techniques and effects of powder characteristics on part proprties in powder-bed fusion processes, Virtual Phys. Prototyp. 12 (1) (2017) 3–29.
[10] A. Simchi, The role of particle size on the laser sintering of Iron powder, Metall. Mater. Trans. B Process Metall. Mater. Process. Sci. 35B (2004) 937–948.
[11] A. Simchi, Direct laser sintering of metal powders: mechanism, kinetics and microstructural features, Mater. Sci. Eng. A 428 (2006) 148–158.
[12] L. Haferkamp, L. Haudenschild, A. Spierings, K. Wegener, K. Riener, S. Ziegelmeier, G. Leichtfried, The influence of particle shape, powder Flowability, and powder layer density on part density in laser powder bed fusion, Metals 11 (418) (2021).
[13] B. Liu, R. Wildman, C. Tuck, I. Ashcroft, R. Hague, Investigation the Effect of Particle Size Distribution on Processing Parameters Optimisation in Selective Laser Melting Process, Loughborough University, Additive Manufacturing Group, 2011.
[14] M. Tang, P. Pistorius, Oxides, porosity and fatigue performance of AlSi10Mg parts produced by selective laser melting, Int. J. Fatigue 94 (2017) 192–201.
[15] A. Strondl, O. Lyckfeldt, H. Brodin, U. Ackelid, Characterization and control of powder properties for additive manufacturing, JOM 67 (2015) 549–554.
[16] M. Ansari, A. Mohamadizadeh, Y. Huang, V. Paserin, Laser directed deposition of water-atomized iron powder: process optimization and microstructure of single-tracks, Opt. Laser Technol. 112 (2019) 485–493.
[17] E. Jelis, M. Clemente, S. Kerwien, N. Ravindra, R. Hespos, Metallurgical and mechanical evaluation of 4340 steel produced by direct metal laser sintering, JOM 67 (3) (2015) 582–589.
[18] A. Raza, C. Pauzon, E. Hryha, A. Markstrom, P. Foret, Spatter oxidation during laser powder bed fusion of alloy 718: dependence on oxygen content in process atmosphere, Addit. Manuf. 48 (2021), 102369.
[19] T. Fedina, J. Sundqvist, A. Kaplan, Spattering and oxidation phenomena during recycling of low alloy steel powder in laser powder bed fusion, Mater. Today Commun. 27 (2021), 102241.
[20] A. Raza, T. Fiegl, I. Hanif, A. Markström, M. Franke, C. Körner, E. Hryha, Degradation of AlSi10Mg powder during laser based powder bed fusion processing, Mater. Des. 198 (2021), 109358.
[21] C. Schwerz, A. Raza, X. Lei, L. Nyborg, E. Hryha, H. Wirdelius, In-situ detection of redeposited spatter and its influence on the formation of internal flaws in laser powder bed fusion, Addit. Manuf. 47 (2021), 102370.
[22] C. Zhuoer, A. Raza, E. Hryha, Influence of part geometry on spatter formation in laser powder bed fusion of Inconel 718 alloy revealed by optical tomography, J. Manuf. Process. 81 (2022) 680–695.
[23] C. Pauzon, A. Raza, E. Hryha, P. Foret, Oxygen balance during laser powder bed fusion of alloy 718, Mater. Des. 201 (2021).
[24] M. Haines, N. Peter, S. Babu, E. Jagle, In-situ synthesis of oxides by reactive process atmosphere during L-PBF of stainless steel, Addit. Manuf. no. 33 (2020).

[25] D.-R. Eo, S. Chung, J. Jeon, J.-W. Cho, Melt pool oxidation and reduction in powder bed fusion, Addit. Manuf. no. 41 (2021).

[26] E. Hryha, E. Dudrova, L. Nyborg, On-line control of processing atmospheres for proper sintering of oxidation-sensitive PM steels, J. Mater. Process. Technol. 212 (2012) 977–987.

[27] C. Gierl-Mayer, Reactions between ferrous powder compacts and atmospheres during sintering - an overview, Powder Metall. 63 (4) (2020) 237–253.

[28] E. Hryha, J. Wendel, Effect of heating rate and process atmosphere on the thermodynamics and kinetics of the sintering of pre-alloyed water-atomized powder metallurgy steels, J. Am. Cerm. Soc. 102 (2019) 748–756.

[29] L. Cordova, T. Bor, M.M. de Smit, M. Campos, T. Tinga, Measuring the spreadability of pre-treated and moisturized powders for laser powder bed fusion, Addit. Manuf. 32 (2020), 101082.

[30] Z. Snow, R. Martukanitz, S. Joshi, On the development of powder spreadability metrics and feedstock requirements for powder bed fusion additive manufacturing, Addit. Manuf. 28 (2019) 78–86.

[31] C. Hulme-Smith, V. Hari, P. Mellin, Spreadability testing of powder for additive manufacturing, BHM Berg- und Huttenmännische Monatshefte 166 (1) (2021) 9–13.

[32] S. Ziegelmeier, P. Christou, F. Wöllecke, C. Tuck, R. Goodridge, R. Hague, E. Krampe, E. Wintermantel, An experimental study into the effects of bulk and flow behavior of laser sintering polymer powder on resulting part properties, J. Mater. Process. Technol. 215 (2015) 239–250.

[33] L. Cordova, M. Campos, T. Tinga, Revealing the effects of powder reuse for selective laser melting by powder characterization, JOM 71 (3) (2019) 1062–1072.

[34] A. Mussatto, R. Groarke, A. O'Neill, M. Obeidi, Y. Delaure, D. Brabazon, Influences of powder morphology and spreading parameters on powder bed topography uniformity in powder bed fusion metal additive manufacturing, Addit. Manuf. 38 (2021), 101807.

[35] L. Marchettie, C. Hulme-Smith, Flowability of steel and tool steel powders: a comparison between testing methods, Powder Technol. 384 (2021) 402–413.

[36] M. Krantz, H. Zhang, J. Zhu, Characterization of powder flow: static and dynamic testing, Powder Technol. 194 (3) (2009) 239–245.

[37] A. Spierings, M. Voegtlin, T. Bauer, K. Wegener, Powder flowability characterisation methodology for powder-bed-based metal additive manufacturing, Progr. Add. Manufact. 1 (2016) 9–20.

[38] L. Haferkamp, A. Spierings, M. Rusch, D. Jermann, M. Spurek, K. Wegener, Effect of particle size on monomodal 316L powder on powder layer density in powder bed fusion, Progr. Add. Manufact. 6 (2021) 367–374.

[39] A. Alexander, B. Chaudhuri, A.-M. Faqih, F. Muzzio, C. Davies, M. Tomassone, Avalanching flow of cohesive powders, Powder Technol. 164 (1) (2006) 13–21.

[40] W. Hearn, E. Hryha, S. Bengtsson, L. Nyborg, Processability & Microstructure of Fe-C system via L-PBF, EuroPM Proc. 2019 (2019).

[41] C. Schneider, W. Rasband, K. Eliceiri, NIH image to ImageJ: 25 years of image analysis, Nat. Methods (2012) 671–675.

[42] D. Schulze, Powders and Bulk Solids: Behavior, Characterization, Storage and Flow, Springer Berlin, Heidelberg, 2008.

[43] Z. Young, M. Qu, M. Coday, Q.H.S. Guo, L. Escano, K. Fezzaa, L. Chen, Effect of particle size distribution with efficient packing on powder Flowability and Selevtive laser melting process, Materials 15 (705) (2022).

[44] J. Weaver, J. Whiting, V. Tondare, C. Beauchamp, M. Peltz, J. Tarr, T. Phan, M. Alkan Donmez, The effects of particle size distribution on the rheological properties of the powder and the mechanical properties of additively manufactured 17-4 PH stainless steel, Addit. Manuf. 39 (2021).

[45] M. Khorasani, A. Ghasemi, M. Leary, E. Sharabian, L. Cordova, I. Gibson, S. Bateman, M. Brandt, B. Rolfe, The effect of absorption ratio on meltpool features in laser-based powder bed fusion of IN718, Opt. Laser Technol. 153 (2022), 108263.

[46] R. Groarke, C. Danilenkoff, S. Karam, E. McCarthy, B. Michel, A. Mussatto, J. Sloane, A. O'Neill, R. Raghavendra, D. Brabazon, 316L stainless steel powders for additive manufacturing: relationships of powder rheology, size, size distribution to part properties, Materials 13 (5537) (2020).

[47] K. Riener, N. Albrecht, S. Ziegelmeier, R. Ramakrishnan, L. Haferkamp, A. Spierings, G. Leichtfried, Influence of particle size distribution and morphology on the properties of the powder feedstock as well as of AlSi10Mg parts produced by laser powder bed fusion (LPBF), Addit. Manuf. 34 (2020), 101286.

[48] B. Chavez Montes, J. Martinez-Alejo, H. Lozano-Perez, J. Gumy, D. Zemlyanov, M. Carvajal, A surface characterization platform approach to study Flowability of food powders, Powder Technol. 357 (2019) 269–280.

[49] M. Adani, R. Dehghani, M. Karamooz-Ravari, R. Mirzaeifar, J. Ni, A study on the effect of energy input on spatter particles creation during selective laser melting process, Addit. Manuf. 20 (2018) 33–43.

[50] H. Gruber, M. Henriksson, E. Hryha, L. Nyborg, Effect of powder recycling in Electron beam melting on the surface chemistry of alloy 718 powder, Metall. Mater. Trans. A 50 (2019) 4410–4422.

[51] D. Gaskell, Introduction to the Thermodynamics of Materials, fifth edition, Taylor & Francis, New York, 2008.

[52] M. Hilzenthaler, F. Scherm, H. Daoud, U. Glatzel, In-situ decarburization and deoxidation during laser powder bed fusion of water-atomized steel C35, Powder Technol. 412 (2022), 117973.

[53] C. Gierl-Mayer, M. Jaliliziyaean, D.H.S. Bengtsson, Dilatometry of PM carbon steels in different atmospheres - Deoxidation effects, in: Proceedings Euro PM2009, 2009.

[54] H. Danninger, C. Gierl-Mayer, S. Kremel, G. Leitner, K. Jaenicke-Roessler, Y. Yu, Degassing and Deoxidation processes during sintering of unalloyed and alloyed PM steels, Powd. Metall. Progr. 2 (3) (2002) 125–140.

[55] T. Nakamoto, N. Shirakawa, Y. Miyata, H. Inui, Selective laser sintering of high carbon steel powders studied as a function of carbon content, J. Mater. Process. Technol. 209 (2009) 5653–5660.

[56] S. Das, Physical aspects of process control in selective laser sintering of metals, Adv. Eng. Mater. 5 (10) (2003) 701–711.

[57] A. Bobel, L.G. Hector Jr., I. Chelladurai, A. Sachdev, T. Brown, W. Poling, R. Kubic, B. Gould, C. Zhao, N. Parab, A. Greco, T. Sun, In situ synchrotron X-ray imaging of 4140 steel laser powder bed fusion, Materialia 6 (2019) 1–10.